Geophysical Research Letters

RESEARCH LETTER
10.1029/2025GL116467

Statistical Distribution of Dawnside Auroral Polarization Streams

Jiang Liu[1,2], Colin Forsyth[3], L. R. Lyons[2], Chih-Ping Wang[2], Vassilis Angelopoulos[1], Andrei Runov[1], Sheng Tian[2], Yangyang Shen[1], Johnathan K. Burchill[4], and S. Milan[5]

[1]Department of Earth and Space Sciences, University of California, Los Angeles, CA, USA, [2]Department of Atmospheric and Oceanic Sciences, University of California, Los Angeles, CA, USA, [3]Department of Space and Climate Physics, Mullard Space Science Laboratory, University College London, Dorking, UK, [4]Department of Physics and Astronomy, University of Calgary, Calgary, AB, Canada, [5]School of Physics & Astronomy, University of Leicester, Leicester, UK

Key Points:

- Dawnside auroral polarization streams (DAPS) appear more often inside a dark ionosphere than a sunlit ionosphere
- The occurrence of DAPS depends on magnetic local time and geomagnetic activity in a complicated yet comprehensible manner
- The signature of embedded Region 2 currents is more prominent when DAPS are present

Supporting Information:

Supporting Information may be found in the online version of this article.

Correspondence to:

J. Liu,
jliu@igpp.ucla.edu

Citation:

Liu, J., Forsyth, C., Lyons, L. R., Wang, C.-P., Angelopoulos, V., Runov, A., et al. (2025). Statistical distribution of dawnside auroral polarization streams. *Geophysical Research Letters*, *52*, e2025GL116467. https://doi.org/10.1029/2025GL116467

Received 10 APR 2025
Accepted 12 JUN 2025

Abstract Dawnside auroral polarization streams (DAPS) are fast eastward flows in the dawn convection cell of Earth's ionosphere. With a steep flow gradient near the interface between Region 1 and 2 currents and a peak poleward of it, DAPS were suggested to be responsible for instabilities and dramatic events in the magnetosphere-ionosphere (M-I) system. To predict these events, it is important to investigate when and where DAPS prefer to occur and how they are related to other M-I phenomena. We conduct this investigation statistically using 10 years of Swarm data and find that DAPS under sunlit and dark ionospheric conditions exhibit different dependencies on magnetic local times and geomagnetic activities, reflecting a complicated interplay between magnetotail dynamics and ionospheric conductance. The statistical results also reveal a strong correlation between DAPS and embedded Region 2 currents. These findings provide new insights into the DAPS generation mechanism.

Plain Language Summary The dawnside auroral polarization stream is a unique type of plasma wind in Earth′s high-latitude ionosphere. These streams play a key role in shaping the aurora and affecting how energy enters from space into the atmosphere. In this study, we explore when and where these streams are most likely to occur. The results not only help us better understand what causes them but also increase the ability to predict space weather events related to them, such as variations in atmosphere temperature.

1. Introduction

The Dungey (1961) cycle is a basic energy circulation mode of Earth's magnetosphere-ionosphere system. This circulation leads to plasma flow loops in the polar ionosphere known as the dawn and dusk convection cells. The lower-latitude, sunward parts of the convection cells, which are known as the "return flow", collocate with the auroral zone and lead to the Region 1 and 2 (R1 and R2) currents (Iijima & Potemra, 1976), a global-scale field-aligned current (FAC; a. k. a. Birkeland current) system as illustrated in Figure 1a (see caption for details). Within the same convection cell, R1 and R2 currents are oppositely directed; the interface between them is usually near the peak return flow. This flow peak, which is eastward in the dawn convection cell and westward in the dusk cell, has been termed a Birkeland current boundary flow (BCBF; Archer et al., 2017).

The characteristics of BCBFs are heavily affected by the dynamics of the Birkeland currents. When the upward FAC equatorward of the eastward BCBF (this FAC is the R2 current) gets enhanced, the flow significantly intensifies due to a polarization effect. Such intensified flows were first observed in the region of the Harang (1946) reversal near midnight (Zou et al., 2009) and later were found to exist in the entire dawn convection cell by Liu et al. (2020), who termed them as "dawnside auroral polarization streams" (DAPS), a special type of BCBF. These streams can greatly enhance the energy input from the magnetosphere to the ionosphere in the form of Poynting flux and thus ionospheric Joule heating (Liu et al., 2024). As a result of this, DAPS-caused heating, high-latitude plasma troughs, ion upflow, and air glows appear in the dawn sector ionosphere (Nanjo et al., 2024; Qian & Wang, 2023; Zou et al., 2013), analogous to the well-known subauroral polarization streams (Foster & Vo, 2002) enhancing low-latitude troughs (Anderson et al., 1993; Bao et al., 2023; D. Lin et al., 2021) and causing STEVE (strong thermal emission velocity enhancement; MacDonald et al., 2018) in the dusk sector (Chu et al., 2019). In addition, DAPS are potential drivers of magnetosphere-ionosphere instabilities responsible for dramatic events such as auroral Omega bands (Liu et al., 2018). Therefore, it is important to advance knowledge about their properties and generation mechanism.

10.1029/2025GL116467

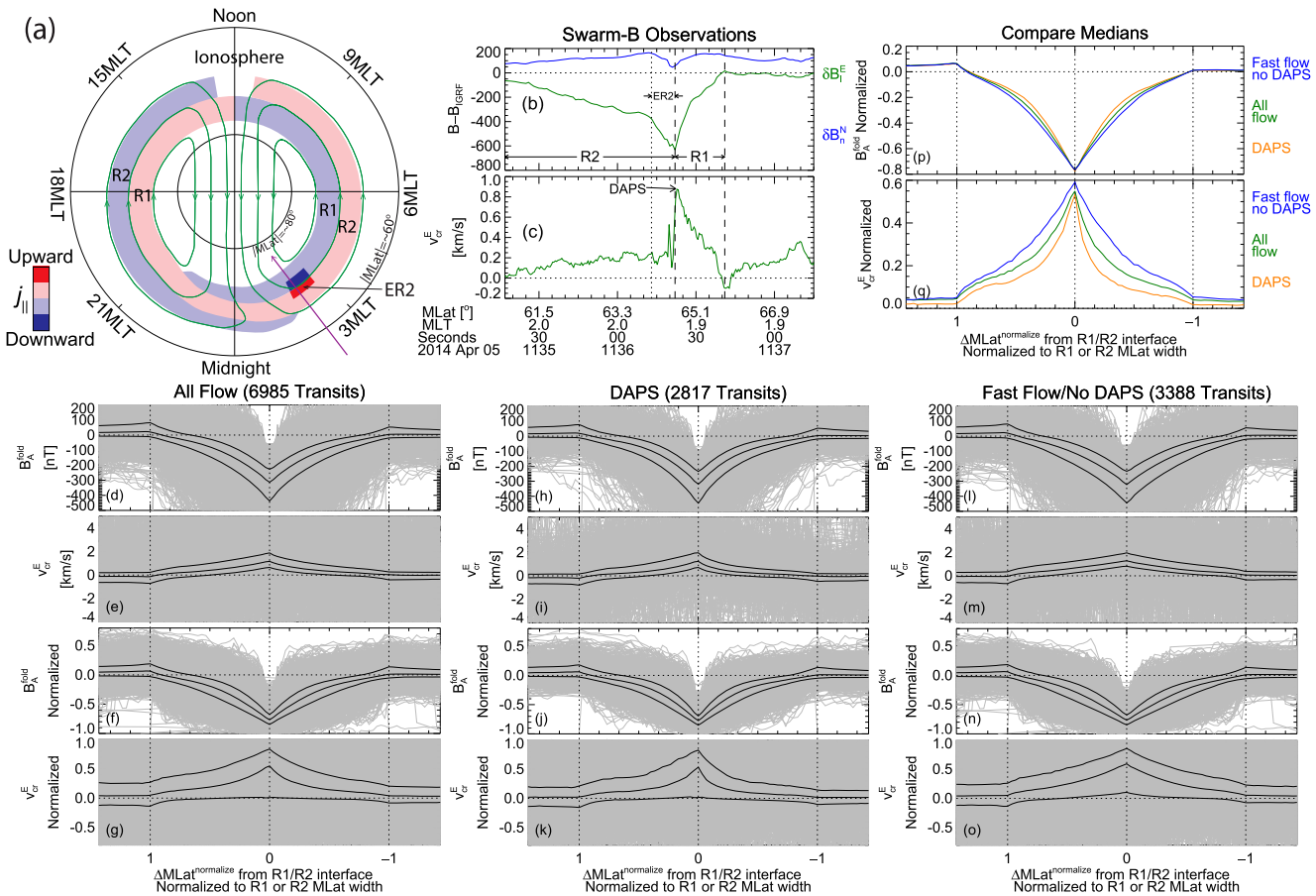

Figure 1. (a) Illustration of the locations of region 1 and 2 currents and the two cell convection in the ionosphere. Pink/light blue: upward/downward field-aligned currents. Red/dark blue: enhanced upward/downward FACs—the embedded R1/R2 FACs (Liu et al., 2021). Green curves: plasma bulk flow lines with arrows indicating their direction; the two loops formed by the curves are the two convection cells (Dungey, 1961). Purple line with an arrow: schematic track of Swarm-B spacecraft giving measurements in (b-c) around 1136UT, 5 April 2014. (b) Components of the perturbation magnetic field vector after the International Geomagnetic Reference Field have been subtracted. Vertical dashed lines indicate the boundaries of R1 and R2 currents. The vertical dotted line indicates the boundaries of the ER2 FACs. Green/blue curves: maximum/minimum variance component of the horizontal magnetic field, approximately eastward/northward. The range for computing the maximum and minimum variance directions is between the first and last vertical dashed lines. (c) Ion bulk flow, cross-track component, approximately eastward. (d–o) Superposed epoch analysis of our various data sets, as indicated on top of each column (see Section 2). The horizontal axis represents the normalized magnetic latitudinal distance from the R1/R2 interface. Poleward (Equatorward) of the R1/R2 interface, the latitudinal distance is normalized by the latitudinal width of the R1 (R2) current. Each gray profile is from a Swarm transit of the return flow region. (d, h, l, f, j, and n) The maximum variance component (approximately east-west) of the horizontal perturbation magnetic field. Many magnetic field profiles have been folded horizontally and/or vertically, so all profiles (gray curves) follow increasing magnetic latitude from left to right of the plots and always show a valley around the reference position 0, the R1/R2 interface. (e, i, m, g, k, and o) The modified cross-track (approximately eastward) ion bulk flow. (f, g, j, k, n and o) Each gray profile has been normalized by its peak-to-peak value within the plot range before superposing. In each of the superposed panels, the three black curves are the median and two quartiles of the gray curves. In panel 1p (1q), the medians in panel 1f–1n (1g, 1k, and 1o) are presented together.

The R2 current enhancement related to DAPS is often concentrated in the R2 range's poleward portion; this concentration is termed an embedded R2 (ER2) current (Liu et al., 2021). The enhancement has two effects as explained by Liu et al. (2020): (a) its closure requires an enhanced equatorward Pederson current and the associated polarization electric field immediately poleward of it; (b) the downward precipitating electrons carried by the enhanced upward FAC lead to high conductance prohibiting a significant electric field (see Figure 2 of Liu et al. (2020)). Most electric fields of the return flow region will thus become intensified poleward of the Region 2 FAC (to complete the potential drop of the return-flow region), where the conductance is relatively low. This concentration further enhances the polarization electric field. This effect should be more pronounced in a dark ionosphere than in a sunlit ionosphere because the conductance contrast between precipitation and no-precipitation regions is more pronounced in a dark ionosphere. Once the equatorward-pointing electric field is enhanced, it drives an enhanced eastward plasma drift, which is the DAPS, with a stark contrast to the lack of flow

10.1029/2025GL116467

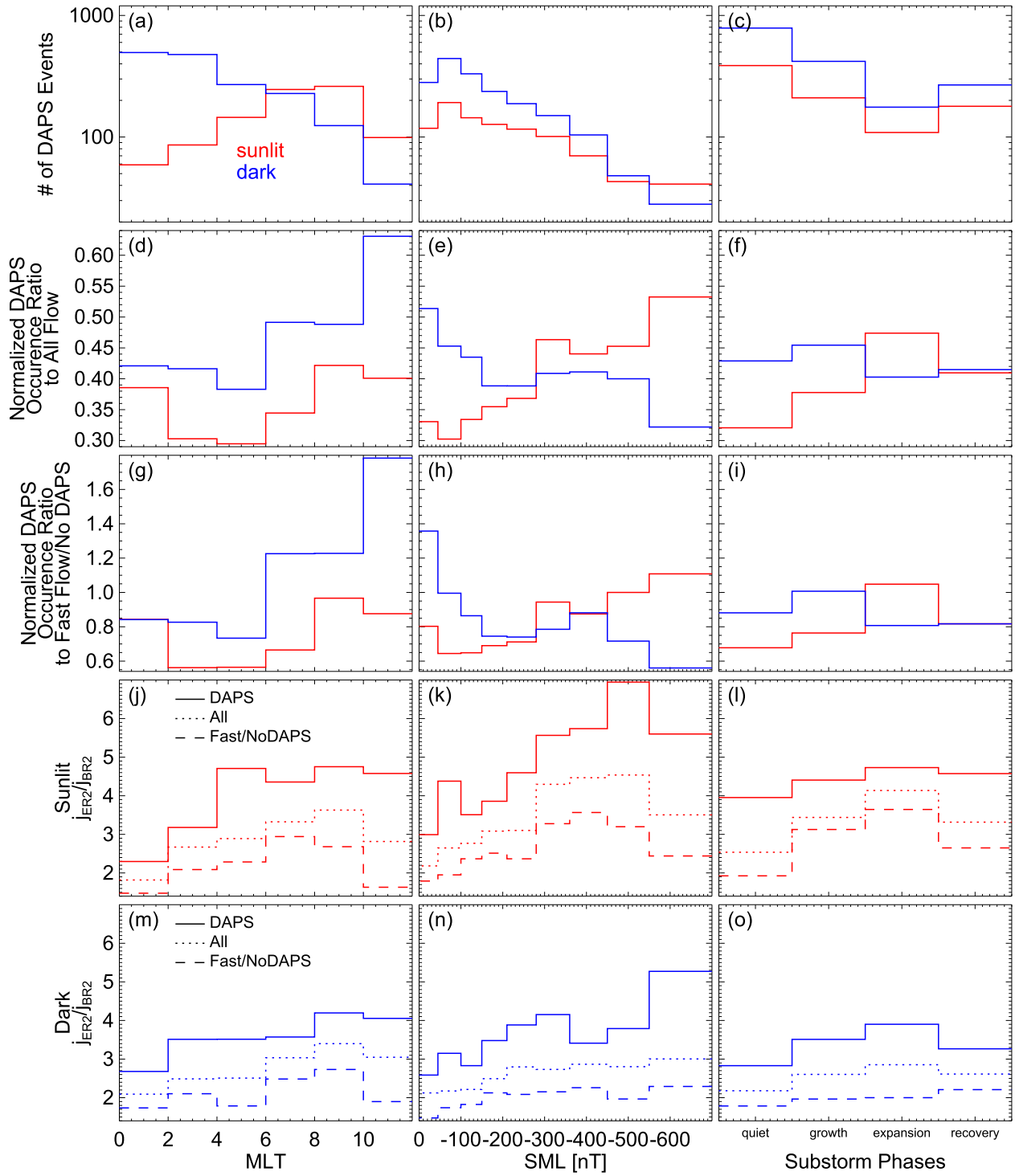

Figure 2. Statistical dependence of (a–c) the number of return-flow transits with Dawnside auroral polarization streams (DAPS), (d–i) the normalized occurrence ratio of DAPS, and (j–o) the medians of current density ratios—that near the R1/R2 interface over that of the background R2 current—on (a, d, g, j, and m) magnetic local time, (b, e, h, k, and n) the SML index, and (c, f, i, l, and o) substorm phases, presented as histograms with bins of the three parameters. In all panels of the left two columns, the width of each step of the histograms indicates the bin size of MLT or SML. In the right-most column, the width only indicates a particular substorm phase (or quiet condition). In the second (third) row, the number of DAPS transits is normalized by the number of all-flow (fast flow/no DAPS) transits. In the fourth and fifth rows, these groups of transits are represented by different line styles as indicated in panel 2j and 2m. The red (blue) histogram represents the sunlit (dark) condition.

equatorward of the R1/R2 interface (Figures 1b and 1c). Because of this contrast, a DAPS shows a steep flow gradient near the interface (Figure 1c). The contrast and gradient are the most indicative signatures distinguishing DAPS from other BCBFs.

The observed features of DAPS and the FAC-related polarization driving them have been reproduced in numerical simulations (Gkioulidou et al., 2009; Wang et al., 2018; D. Lin et al., 2022). In the simulations, the enhanced R2 FAC arises from the deceleration and diversion of magnetotail fast flows when they approach the inner edge of the plasma sheet (e.g., Birn et al., 1999; Yang et al., 2010). These fast flows, also known as "bursty bulk flows" (Angelopoulos et al., 1992), likely result from near-earth tail reconnection (e.g., Sitnov et al., 2009) and propagate earthward due to magnetic forcing (Li et al., 2011; Liu et al., 2014).

To summarize, previous suggestions of DAPS generation imply that they are associated with nightside phenomena during strong geomagnetic activity (when convection is intense) and enhanced R2 currents (including the ER2 current). However, these suggestions have been verified only by a few case studies. In this paper, we test their validity with a comprehensive statistical study, by which we will find when and where they prefer to occur and whether they are associated with ER2 currents.

2. Statistical Data Sets

Our statistical database comes from the Swarm mission, which was launched in 2013 and consists of three identical, polar-orbiting spacecraft: A, B, and C. Swarm A and C are at ~460 km altitude, whereas Swarm B is at ~530 km altitude. Each of the spacecraft carries a fluxgate magnetometer which measures the magnetic field vector (Merayo et al., 2008) and thermal ion imagers (TII) measuring ion bulk velocity in the horizontal and vertical planes (Knudsen et al., 2017). Because the velocity component parallel to the spacecraft trajectory is unreliable (Burchill & Knudsen, 2022), we restrict our analysis of horizontal flows to the cross-track component, which is approximately east-west aligned in the return flow region. On timescales longer than a few months, the three Swarm spacecraft uniformly sample the return flow in local time. We use all three spacecraft's data from December 2013 to September 2023 for our study.

First, we determine the ranges of R1 and R2 currents by applying the automated algorithm of Liu et al. (2022) to Swarm′s magnetic field measurements. Each interval containing both the R1 and R2 ranges marks a Swarm transit of the return flow region. Then we identify transits of the dawn convection cell as intervals when the R1 FAC is downward (toward the ionosphere) and the R2 FAC is upward. Here the FAC directions are given by the slopes of the east-west magnetic field component (Figure 1b; see also Liu et al., 2024). All the transits with any flow data available over the return flow region of the dawn convection cell make up our "all-flow" data set (6,985 transits).

Figures 1d–1g present a superposed "epoch" analysis of the magnetic field and flow variations of the all-flow transits, with the "epoch" being the normalized latitudinal distance from the R1/R2 interface (normalized by the latitudinal width of R1 or R2 current). In Figures 1f and 1g, we also normalize each profile by its peak-to-peak magnitude before superposing. The magnetic field in Figures 1d and 1f is the maximum variance component (B_A; approximately east-west aligned), which has been folded (multiplying ± 1) to always show a dip at the R1/R2 interface (see Liu et al., 2022 for how this component is defined). The flow in Figures 1e and 1g is the modified cross-track component v_{cr}^E—we have multiplied the original data by -1 if the spacecraft is flying southward so a positive v_{cr}^E is approximately eastward in the return-flow region. Figures 1e and 1g show statistical peaks of v_{cr}^E at the R1/R2 interface, as expected from BCBFs.

Next, we select DAPS transits by applying the fully automated algorithm of Liu et al. (2024) to the all-flow data set. We briefly describe the essence of this algorithm: it looks for a steep v_{cr}^E gradient near the R1/R2 interface with an eastward peak poleward of it. The v_{cr}^E jump over the gradient must be more than half the maximum v_{cr}^E of the return flow region; the DAPS flow peak must be more than 0.5 km/s. These criteria were based on examination of many DAPS events. Compared to previous statistical studies, which identify any fast eastward flow near the dawnside R1/R2 interface as a DAPS (Qian & Wang, 2023), this algorithm emphasizes DAPS' drastic flow change across the interface, a key signature for their potential role in instabilities (Liu et al., 2018). It gives 2,817 transits containing DAPS. Figures 1h–1k present the superposed magnetic field and flow of these transits.

The DAPS criterion for a flow jump implies the selected flows are fast, so the statistical trends from the DAPS data set may contain features of general fast flows. To isolate the effects of DAPS' nature from those caused just by a flow being fast, we prepare a comparison fast-flow data set. From the "all-flow" data set, we select every transit with any v_{cr}^{E} data point in the return flow region exceeding a criterion v_c. Then we exclude the transits already contained in the DAPS data set. To fairly compare the statistical results from this fast-flow/no-DAPS data set with the DAPS data set, we choose v_c to be 0.85 km/s. This choice makes the median of the maximum v_{cr}^{E} over the return flow region the same for the two data sets (2.07 km/s), so any difference in the statistical trends from these two data sets should be due to DAPS' nature instead of flow speed. Figures 1l–1o display the superposed epoch analysis for the resultant fast-flow/no-DAPS data set (3,388 transits).

In Figure 1q, we overlay the median flow profile of the three datasets. The DAPS profile clearly shows a steeper v_{cr}^{E} gradient immediately equatorward of the R1/R2 interface than the other two profiles. This indicates that our selection algorithm has successfully identified DAPS.

In addition to Swarm data, we will also use the SuperMAG auroral low (SML) index to quantify the geomagnetic activity level (equivalent to the AL index; see Newell & Gjerloev, 2011). This index, however, cannot fully reflect M-I activities. For example, the substorm growth phase shows a low SML but already involves significant convection. We thus also use substorm phases as a parameter in our study. First, we apply the Forsyth et al. (2015) algorithm, which gives intervals of substorm expansion and recovery phases. Then we designate the periods within 1 hour after recovery phases as substorm aftermaths and 72 min before expansion phases as growth phases. Here 72 min is the typical duration of substorm growth phases (e.g., Iyemori, 1980). All other intervals are termed "quiet." We avoid any overlap in the determined periods—those mentioned later always give way to those mentioned earlier.

3. Results

As suggested by previously proposed generation scenarios, DAPS are associated with enhanced convection originating from the nightside magnetosphere and a conductance difference in the ionosphere caused by electron precipitation (see Section 1). The former implies possible dependence of DAPS properties on magnetic local time, activity level (proxied by SML index), and substorm phases. The latter suggests a dependence on the illumination state of the ionosphere because the precipitation-caused conductance difference is more pronounced in a dark ionosphere than in a sunlit one. In this section, we will investigate the statistical DAPS dependence on all these parameters.

First, we determine whether each Swarm transit is within a sunlit or dark ionosphere using a criterion of 90°50′ solar zenith angle (Jacobson et al., 2011). We applied this criterion to the time when Swarm is at the R1/R2 interface and found that the all-flow, DAPS, fast flow/no DAPS data sets contain 979, 2,708, and 1,316 (1,838, 4,277, and 2,072) sunlit (dark) transits, respectively. For all data sets, there are more transits under dark conditions than under sunlight. This arises largely due to a bias in TII operations favoring night-side measurements (Burchill & Knudsen, 2022).

3.1. Occurrence

First, we examine DAPS occurrence under different conditions. In Figures 2a–2c, we plot the number of transits with DAPS identified. The numbers within different condition bins are presented as histograms. Figure 2a shows that when the ionosphere is dark, more DAPS are observed in nightside MLTs than in dayside MLTs. The preference under sunlight is opposite. This is because nightside MLTs are more often under darkness than dayside MLTs, which are more often under sunlight. Figures 2b and 2c show that more DAPS are observed during less active conditions than during more active conditions, likely because the magnetosphere-ionosphere system is more often quiet.

To remove biases associated with different conditions' intrinsic preferences (as above) and instrument operations, we divide the number of DAPS encounters in each condition bin of Figures 2a–2c by the number of "all-flow" transits in that bin to get normalized occurrence rates (Figures 2d–2f). As Figure 2d illustrates, the DAPS occurrence rate in all MLTs is higher for a dark ionosphere than for a sunlit ionosphere. In general, the occurrence rate is higher for dayside MLTs than for nightside MLTs; this preference is more obvious under dark conditions than under sunlight. In Figure 2e, these two conditions show opposite DAPS dependences on SML—in the dark

(sunlit) ionosphere, DAPS have higher occurrence rates under low (high) activity levels than under high (low) activity levels. In the dark ionosphere, the DAPS occurrence rate is highest during the substorm growth phase (Figure 2f). In a sunlit ionosphere, its occurrence rate increases from quiet periods to the growth phase, maximizes during the expansion phase, and drops during the recovery phase, when it is still higher than for the quiet and growth phases.

In Figures 2g–2i, we divide the number of DAPS encounters in each condition bin by the number of "fast flow/no DAPS" transits in that bin. This removes the conditions' bias as well as any effect due to the flow just being fast. All the dependencies revealed in Figures 2g–2i are the same as those in Figures 2d–2f.

3.2. Relationship to Embedded Region 2 Currents

Next, we examine whether DAPS are indeed correlated with ER2 currents. The median of superposed magnetic field profiles in Figure 1p already provides evidence that DAPS are related to ER2 currents. For the transits with DAPS, the slope of the east-west field near the R1/R2 interface is apparently steeper than that farther from it, indicating a higher current density. This is the defining signature of embedded R1 and R2 currents (Liu et al., 2021). This signature for the median profile of the "all flow" transits is visible but not as apparent, and it is hardly visible for the "fast flow/no DAPS" transits.

To further confirm the correlation between DAPS and ER2 currents, for each transit we compute the ratio between the average R2 current density near the R1/R2 interface (j_{ER2}) and that far from the interface (j_{BR2}). Both are computed as the B_A change divided by the latitudinal difference over a range (assuming the spacecraft is crossing an east-west aligned sheet current; see Luhr et al., 1996)—the range for the former is from the R1/R2 interface to the latitudinal middle point of the R2 range; the range for the latter is from the middle point to the equatorward boundary of the R2 current. A higher current density ratio should indicate a more prominent ER2 signature.

In Figures 2j–2o, we plot the medians of this ratio for transits under different conditions. For all conditions, the median ratio is highest for the transits with DAPS identified and lowest for the "fast flow/no DAPS" transits. The median ratio for "all flow" transits (which contains the DAPS transits) is always between those for the other two data sets. For all data sets under both dark and sunlit conditions, the median ratio generally increases with SML (Figures 2k and 2n). It is lowest during quiet periods, higher during the substorm growth phase, and maximized during the expansion phase (Figures 2l and 2o). The median ratio is generally higher for dayside MLTs than for nightside MLTs (Figures 2j and 2m) and higher for the sunlit ionosphere than for the dark ionosphere.

3.3. Results With Split Conditions

In Figure 2, we have not separated different geomagnetic activities when investigating the dependence on MLT and vice versa. In the supporting material (Figures S1–S4 in Supporting Information S1), we split the data sets into low and high activity levels and dayside and nightside MLTs and repeat the statistical study. Most of the split results are in qualitative agreement with those in Figure 2, but they also show some notable features: DAPS' occurrence rate is always higher in a dark ionosphere than a sunlit ionosphere (Figures S1a, S1b, S2a, S2b, S3a, and S3c in Supporting Information S1) with one exception—nightside MLTs under high activity level (SML $< \sim -350$ nT; Figures S4a and S4c in Supporting Information S1). During low geomagnetic activity levels, DAPS' occurrence rate on the nightside is comparable to that on the dayside for both sunlit and dark conditions (Figures S1a and S1b in Supporting Information S1). During high activity levels (Figures S2a and S2b in Supporting Information S1), their preference for the dayside is more prominent than the overall trends in Figures 2d and 2g. When the dayside MLTs are dark, DAPS occur more often during more active geomagnetic conditions (Figures S3a and S3c in Supporting Information S1), opposite to the overall trends in Figures 2e and 2h (so they mainly reflect the nightside trends in Figures S4a and S4c in Supporting Information S1). Consistently on the dark dayside, the DAPS occurrence rate is higher during the substorm expansion phase than during the quiet and growth phases and it is even higher during the recovery phase (Figures S3b and S3d in Supporting Information S1). On the dark nightside, the occurrence rate is highest during the growth phase (Figures S4b and S4d in Supporting Information S1), which shows up in the overall trends in Figures 2f and 2i. Under sunlight, the highest occurrence rate is during the expansion phase for both dayside and nightside MLTs. The second highest, however, is during the recovery phase for dayside MLTs (Figures S3b and S3d in Supporting Information S1) but during the growth phase for nightside MLTs (Figures S4b and S4d in Supporting Information S1). In the next section, we discuss the implications of these features.

4. Findings and Implications

Our results reveal that in general, DAPS preferentially occur under dark conditions, during dayside local times, amid elevated geomagnetic activity, and in the presence of an embedded Region 2 current.

Under specific conditions, however, the statistical trends show more complicated variations. We summarize them and speculate their implications on DAPS generation in the following.

1. Under most conditions, DAPS prefer to occur inside a dark ionosphere than in a sunlit one. This indicates that the ionospheric conductance difference caused by electron precipitation is important for DAPS generation (see Section 1)—the relative conductance difference caused by the precipitation is larger in a dark ionosphere than in a sunlit one because the latter has a larger base conductance caused by solar extreme ultraviolet radiation. On the other hand, the sunlit ionosphere still hosts a significant number of DAPS, indicating that the closure of the enhanced R2 current can lead to DAPS without much help from large relative conductance differences, which the sunlit ionosphere lacks.
2. The occurrence of DAPS appears to prefer dayside MLTs rather than nightside MLTs, especially during geomagnetic active times. This preference is not against previous suggestions that the DAPS generation mechanism originates from fast plasma flows in the magnetotail. The enhanced R2 current due to these flows, which were suggested to drive DAPS, extends to dayside MLTs (Y. Lin et al., 2021), so we expect DAPS to occur on the dayside too. In addition, the enhancement of the global uniform M-I convection has also been suggested to lead to DAPS (Liu et al., 2020); this convection has no preference for the nightside. The reason why DAPS appear less often on the nightside is likely due exactly to the nightside origin of perturbations—because most plasma sheet perturbations originate from the nightside, the nightside auroral zone should be more perturbed than the dayside (a major portion of the auroral zone is connected to the plasma sheet). Perturbations other than DAPS (e.g., auroral bulging) likely disrupt the ionospheric conditions favoring DAPS generation, so DAPS occur less often. We expect this effect to be more prominent during active times than during quieter times, and so is the DAPS preference for the dayside (Section 3.3).
3. In a sunlit ionosphere or a dark dayside ionosphere, DAPS occur more often when the geomagnetic activity level is higher (as represented by the SML index). This trend is consistent with previous speculations that DAPS are driven by active time convection.
4. In a dark nightside ionosphere, DAPS' occurrence rate drops as the geomagnetic activity level increases. This trend likely results from the same effect mentioned above due to plasma sheet perturbations originating from the nightside—under more active conditions, there are more perturbed ionospheric flows disrupting DAPS signatures. This effect also impacts the sunlit nightside ionosphere (comparing Figures S4a and S4b to Figures S3a and S3b in Supporting Information S1), but it is not strong enough to reverse DAPS' occurrence preference for active conditions. This suggests that the ionospheric flow perturbations disrupting DAPS are more pronounced under dark conditions than under sunlight, likely due to polarization driven by large conductance differences (other than those giving rise to DAPS) which only appear under dark conditions. When the geomagnetic activity level is very high (SML < -350 nT), we expect this effect to be very intense, so the DAPS occurrence rate under dark conditions drops below that under sunlight. This is the only exception to the first conclusion of Section 4.
5. Under sunlight, DAPS' occurrence rate is highest during the expansion phase and lowest during quiet conditions, as compared to other substorm phases. This is expected because the magnetosphere-ionosphere convection (including magnetotail fast flows) is most intense during the expansion phase and least intense during the quiet time. The second-highest occurrence rate of DAPS is during the recovery phase for dayside MLTs but during the growth phase for nightside MLTs. This is likely due to the aforementioned nightside perturbations disrupting DAPS signatures. The recovery phase, when the activity level is higher than during the growth phase, should accommodate more such perturbations than the growth phase does, so nightside DAPS' occurrence rate during the recovery phase drops below that during the growth phase.
6. In the dark nightside ionosphere, the DAPS occurrence rate is highest during the substorm growth phase. This indicates that the enhanced M-I convection during the growth phase is already sufficient for DAPS generation (see an example in Liu et al. (2020)). Although the convection is more enhanced during the expansion and recovery phases, other perturbations originating from the nightside plasma sheet may disrupt DAPS generation, so their occurrence rate is not as high as the growth phase. Dayside MLTs are less affected by such disruptions, so the DAPS occurrence rate increases from the quiet and growth phases toward the expansion and recovery phases in the dark dayside ionosphere. The rate maximizes during the recovery phase, possibly due to

one of the following two reasons: (a) the enhanced R2 current (mainly contributed by tail fast flows) takes some time to propagate to the dayside; (b) to some degree, the DAPS-disrupting perturbations originating from the tail impacts the dayside too during the expansion phase, but not during the recovery phase because the activity level has dropped.

7. Under all conditions, the embedded Region 2 current signature is more pronounced when a DAPS is present. This correlation supports previous suggestions that embedded R2 currents are drivers of DAPS (Liu et al., 2021).
8. The ER2 signature is more prominent when the geomagnetic activity level is higher; its prominence increases as a substorm progresses through different phases, from quiet to growth to expansion. These trends are consistent with previous findings about their dependence on geomagnetic activity level (Liu et al., 2022).

The above conclusions and discussions on the DAPS occurrence and their relationship to the M-I current system provide significant insights toward understanding their generation mechanism and predicting their impact on energy transfer and instabilities in the ionosphere and magnetosphere. These implications from our statistical results can be tested by future comprehensive observations and simulations.

Data Availability Statement

The data used in this study are publicly available at the Swarm data site (https://swarm-diss.eo.esa.int/) and the SuperMAG official website (https://supermag.jhuapl.edu/indices/). The version of the Swarm magnetic field data is 0602 and the version of the TII data is 0302. The software employed in this study is available at the SPEDAS software page https://themis.ssl.berkeley.edu/software.shtml and Zenodo: (Liu, 2025).

Acknowledgments
The work at UCLA was supported by NASA Grants 80NSSC23K0903, 80NSSC22K0749, 80NSSC22K0751, 80NSSC22K1012, 80NSSC20K1314, and contract NAS502099 and NSF Grants AGS-2410899, AGS-2247034, AGS-2224108, and AGS-2055192. Colin Forsyth was supported by STFC Grant ST/Y002237/1 and UKSA Grant ST/Y003276/1. Swarm TII data processing was supported in part by the Canadian Space Agency. We thank the Swarm and SuperMAG teams for providing the data used in this study.

References

Anderson, P. C., Hanson, W. B., Heelis, R. A., Craven, J. D., Baker, D. N., & Frank, L. A. (1993). A proposed production model of rapid subauroral ion drifts and their relationship to substorm evolution. *Journal of Geophysical Research*, *98*(A4), 6069–6078. https://doi.org/10.1029/92ja01975

Angelopoulos, V., Baumjohann, W., Kennel, C. F., Coroniti, F. V., Kivelson, M. G., Pellat, R., et al. (1992). Bursty bulk flows in the inner central plasma sheet. *Journal of Geophysical Research*, *97*(A4), 4027–4039. https://doi.org/10.1029/91JA02701

Archer, W. E., Knudsen, D. J., Burchill, J. K., Jackel, B., Donovan, E., Connors, M., & Juusola, L. (2017). Birkeland current boundary flows. *Journal of Geophysical Research: Space Physics*, *122*(4), 4617–4627. https://doi.org/10.1002/2016ja023789

Bao, S., Wang, W., Sorathia, K., Merkin, V., Toffoletto, F., Lin, D., et al. (2023). The relation among the ring current, subauroral polarization stream, and the geospace plume: MAGE simulation of the 31 March 2001 super storm. *Journal of Geophysical Research: Space Physics*, *128*(12), e2023JA031923. https://doi.org/10.1029/2023JA031923

Birn, J., Hesse, M., Haerendel, G., Baumjohann, W., & Shiokawa, K. (1999). Flow braking and the substorm current wedge. *Journal of Geophysical Research*, *104*(A9), 19895–19903. https://doi.org/10.1029/1999JA900173

Burchill, J. K., & Knudsen, D. J. (2022). Swarm thermal ion imager measurement performance. *Earth Planets and Space*, *74*(1), 181. https://doi.org/10.1186/s40623-022-01736-w

Chu, X., Malaspina, D., Gallardo-Lacourt, B., Liang, J., Andersson, L., Ma, Q., et al. (2019). Identifying STEVE's magnetospheric driver using conjugate observations in the magnetosphere and on the ground. *Geophysical Research Letters*, *46*(22), 12665–12674. https://doi.org/10.1029/2019GL082789

Dungey, J. W. (1961). Interplanetary magnetic field and the auroral zones. *Physical Review Letters*, *6*(2), 47–48. https://doi.org/10.1103/PhysRevLett.6.47

Forsyth, C., Rae, I. J., Coxon, J. C., Freeman, M. P., Jackman, C. M., Gjerloev, J., & Fazakerley, A. N. (2015). A new technique for determining substorm onsets and phases from indices of the electrojet (SOPHIE): SOPHIE SUBSTORM ONSETS AND PHASES. *Journal of Geophysical Research: Space Physics*, *120*(12), 10592–10606. https://doi.org/10.1002/2015JA021343

Foster, J. C., & Vo, H. B. (2002). Average characteristics and activity dependence of the subauroral polarization stream. *Journal of Geophysical Research*, *107*(A12), SIA16-1–SIA16-10. https://doi.org/10.1029/2002ja009409

Gkioulidou, M., Wang, C.-P., Lyons, L. R., & Wolf, R. A. (2009). Formation of the Harang reversal and its dependence on plasma sheet conditions: Rice convection model simulations. *Journal of Geophysical Research*, *114*(A7), A07204. https://doi.org/10.1029/2008ja013955

Harang, L. (1946). The mean field of disturbance of polar geomagnetic storms. *Journal of Geophysical Research*, *51*(3), 353–380. https://doi.org/10.1029/TE051i003p00353

Iijima, T., & Potemra, T. A. (1976). The amplitude distribution of field-aligned currents at northern high latitudes observed by Triad. *Journal of Geophysical Research*, *81*(13), 2165–2174. https://doi.org/10.1029/JA081i013p02165

Iyemori, T. (1980). Time delay of the substorm onset from the IMF southward turning. *Journal of Geomagnetism and Geoelectricity*, *32*(5), 267–273. https://doi.org/10.5636/jgg.32.267

Jacobson, L. D., Seaver, A., & Tang, J. (2011). AstroCalc4R: Software to calculate solar zenith angle; time at sunrise, local noon, and sunset; and photosynthetically available radiation based on date, time, and location. *U.S. Department of Commerce, Northeast Fisheries Science Center Reference Document*. Retrieved from https://repository.library.noaa.gov/view/noaa/3867

Knudsen, D. J., Burchill, J. K., Buchert, S. C., Eriksson, A. I., Gill, R., Wahlund, J. E., et al. (2017). Thermal ion imagers and Langmuir probes in the Swarm electric field instruments. *Journal of Geophysical Research: Space Physics*, *122*(2), 2655–2673. https://doi.org/10.1002/2016ja022571

Li, S.-S., Angelopoulos, V., Runov, A., Zhou, X.-Z., McFadden, J., Larson, D., et al. (2011). On the force balance around dipolarization fronts within bursty bulk flows. *Journal of Geophysical Research*, *116*(A5), A00I35. https://doi.org/10.1029/2010JA015884

Lin, D., Sorathia, K., Wang, W., Merkin, V., Bao, S., Pham, K., et al. (2021). The role of diffuse electron precipitation in the formation of subauroral polarization streams. *Journal of Geophysical Research: Space Physics*, *126*(12), e2021JA029792. https://doi.org/10.1029/2021JA029792

Lin, D., Wang, W., Merkin, V. G., Huang, C., Oppenheim, M., Sorathia, K., et al. (2022). Origin of dawnside subauroral polarization streams during major geomagnetic storms. *AGU Advances*, *3*(4), e2022AV000708. https://doi.org/10.1029/2022AV000708

Lin, Y., Wang, X. Y., Fok, M.-C., Buzulukova, N., Perez, J. D., Cheng, L., & Chen, L.-J. (2021). Magnetotail-inner magnetosphere transport associated with fast flows based on combined global-hybrid and CIMI simulation. *Journal of Geophysical Research: Space Physics*, *126*(3), e2020JA028405. https://doi.org/10.1029/2020JA028405

Liu, J. (2025). Data and code for statistical distributions of dawnside auroral polarization streams [Dataset]. *Zenodo*. In *Statistical distribution of dawnside auroral polarization streams*. https://doi.org/10.5281/zenodo.15686341

Liu, J., Angelopoulos, V., Zhou, X.-Z., & Runov, A. (2014). Magnetic flux transport by dipolarizing flux bundles. *Journal of Geophysical Research: Space Physics*, *119*(2), 909–926. https://doi.org/10.1002/2013JA019395

Liu, J., Higuchi, T., Lyons, L. R., Ohtani, S., Wu, J., Zou, Y., et al. (2022). The occurrence of embedded region 1 and 2 currents depends on geomagnetic activity level. *Journal of Geophysical Research: Space Physics*, *127*(11), e2022JA030539. https://doi.org/10.1029/2022JA030539

Liu, J., Lyons, L. R., Wang, C., Ma, Y., Strangeway, R. J., Zhang, Y., et al. (2021). Embedded regions 1 and 2 field-aligned currents: Newly recognized from low-altitude spacecraft observations. *Journal of Geophysical Research: Space Physics*, *126*(6), e2021JA029207. https://doi.org/10.1029/2021JA029207

Liu, J., Lyons, L. R., Archer, W. E., Gallardo-Lacourt, B., Nishimura, Y., Zou, Y., et al. (2018). Flow shears at the poleward boundary of Omega bands observed during conjunctions of Swarm and THEMIS ASI. *Geophysical Research Letters*, *45*(3), 1218–1227. https://doi.org/10.1002/2017gl076485

Liu, J., Lyons, L. R., Knipp, D., Zhang, Q., Wang, C., Shen, Y., et al. (2024). Poynting flux input to the auroral ionosphere: The impact of subauroral polarization streams and dawnside auroral polarization streams. *Journal of Geophysical Research: Space Physics*, *129*(5), e2024JA032605. https://doi.org/10.1029/2024JA032605

Liu, J., Lyons, L. R., Wang, C., Hairston, M. R., Zhang, Y., & Zou, Y. (2020). Dawnside auroral polarization streams. *Journal of Geophysical Research: Space Physics*, *125*(8), e2019JA027742. https://doi.org/10.1029/2019JA027742

Luhr, H., Warnecke, J. F., & Rother, M. K. A. (1996). An algorithm for estimating field-aligned currents from single spacecraft magnetic field measurements: A diagnostic tool applied to freja satellite data. *IEEE Transactions on Geoscience and Remote Sensing*, *34*(6), 1369–1376. https://doi.org/10.1109/36.544560

MacDonald, E. A., Donovan, E., Nishimura, Y., Case, N. A., Gillies, D. M., Gallardo-Lacourt, B., et al. (2018). New science in plain sight: Citizen scientists lead to the discovery of optical structure in the upper atmosphere. *Science Advances*, *4*(3), eaaq0030. https://doi.org/10.1126/sciadv.aaq0030

Merayo, J. M. G., Jørgensen, J. L., Friis-Christensen, E., Brauer, P., Primdahl, F., Jørgensen, P. S., et al. (2008). The Swarm magnetometry package. In *Small satellites for earth observation* (pp. 143–151). Springer.

Nanjo, S., Hofstra, G. A., Shiokawa, K., Shinbori, A., Nozawa, S., & Hosokawa, K. (2024). Post-midnight purple arc and patches appeared on the high latitude part of the auroral oval: Dawnside counterpart of STEVE? *Earth Planets and Space*, *76*(1), 55. https://doi.org/10.1186/s40623-024-01995-9

Newell, P. T., & Gjerloev, J. W. (2011). Evaluation of SuperMAG auroral electrojet indices as indicators of substorms and auroral power. *Journal of Geophysical Research*, *116*(A12), 2011JA016779. https://doi.org/10.1029/2011JA016779

Qian, C., & Wang, H. (2023). A statistical study of ion upflow during periods of dawnside auroral polarization streams and subauroral polarization streams. *Remote Sensing*, *15*(5), 1320. https://doi.org/10.3390/rs15051320

Sitnov, M. I., Swisdak, M., & Divin, A. V. (2009). Dipolarization fronts as a signature of transient reconnection in the magnetotail. *Journal of Geophysical Research*, *114*(A4), 4202. https://doi.org/10.1029/2008JA013980

Wang, C.-P., Gkioulidou, M., Lyons, L. R., & Wolf, R. A. (2018). Spatial distribution of plasma sheet entropy reduction caused by a plasma bubble: Rice convection model simulations. *Journal of Geophysical Research: Space Physics*, *123*(5), 3380–3397. https://doi.org/10.1029/2018ja025347

Yang, J., Toffoletto, F. R., & Song, Y. (2010). Role of depleted flux tubes in steady magnetospheric convection: Results of RCM-E simulations: RCM-E Simulations OF SMC. *Journal of Geophysical Research*, *115*(A5), A00I11. https://doi.org/10.1029/2010JA015731

Zou, S., Lyons, L. R., Nicolls, M. J., Heinselman, C. J., & Mende, S. B. (2009). Nightside ionospheric electrodynamics associated with substorms: PFISR and THEMIS ASI observations: IONOSPHERIC CONVECTION DURING SUBSTORM. *Journal of Geophysical Research*, *114*(A12), A12301. https://doi.org/10.1029/2009JA014259

Zou, S., Moldwin, M. B., Nicolls, M. J., Ridley, A. J., Coster, A. J., Yizengaw, E., et al. (2013). Electrodynamics of the high-latitude trough: Its relationship with convection flows and field-aligned currents. *Journal of Geophysical Research: Space Physics*, *118*(5), 2565–2572. https://doi.org/10.1002/jgra.50120